Sunlight Selective Photodeposition of CoOx(OH)y and NiOx(OH)y on Truncated Bipyramidal BiVO4 for Highly Efficient Photocatalysis

Yannick Hermans, Céline Olivier, Henrik Junge, Andreas Klein, Wolfram Jaegermann, Thierry Toupance

Sun Light Selective Photodeposition of $CoO_x(OH)_y$ and $NiO_x(OH)_y$ on Truncated Bipyramidal $BiVO_4$ for Highly Efficient Photocatalysis

*Yannick Hermans,[1,2] Céline Olivier,[1] Henrik Junge,[3] Andreas Klein,[2] Wolfram Jaegermann[2] and Thierry Toupance[1]**

[1]Université de Bordeaux, Institut des Sciences Moléculaires, UMR 5255 CNRS, 351 Cours de la Libération, 33 405 Talence, France

[2]Technische Universität Darmstadt, Fachbereich Material- und Geowissenshaften, Petersenstr. 23, 64287 Darmstadt, Germany

[3]Leibniz Institute for Catalysis, Albert-Einstein-Strasse 29a, D-18059 Rostock, Germany.

KEYWORDS: Sun light photodeposition, Facet-engineered $CoO_x(OH)_y$- and $NiO_x(OH)_y$-monoclinic scheelite $BiVO_4$ microcrystals, Photocatalysis, Sacrificial water oxidation.

ABSTRACT

Facet-engineered monoclinic scheelite $BiVO_4$ particles decorated with various co-catalysts were successfully synthesized by selective sun light photodeposition of metal or metal oxy(hydroxide) nanoparticles onto the facets of truncated bipyramidal $BiVO_4$ monoclinic crystals co-exposing {010} and {110} facets. X-ray photoelectron spectroscopy, scanning electron microscopy and scanning Auger microscopy revealed that metallic silver (Ag) and cobalt (oxy)hydroxide ($CoO_x(OH)_y$) particles were selectively deposited onto the {010} and {110} facets, respectively, regardless of the co-catalyst amount. By contrast, the nickel (oxy)hydroxide ($NiO_x(OH)_y$) photodeposition depends on the nickel precursor amount with an unprecedented selectivity for 0.1 wt% $NiO_x(OH)_y/BiVO_4$ with a preferential deposition onto the {010} facets and the edges between the {110} facets. Moreover, these noble metal-free heterostructures led to remarkable photocatalytic properties for rhodamine B photodecomposition and sacrificial water oxidation reactions. For instance, 0.2 wt% $CoO_x(OH)_y/BiVO_4$ led to one of the highest oxygen evolution rate, i.e. 1538 $\mu mol.h^{-1}.g^{-1}$, ever described which is ten times higher than that found for bare $BiVO_4$. The selective deposition of cobalt (oxy)hydroxide species onto the more electron-deficient facet of truncated bipyramidal monoclinic $BiVO_4$ particles favors photogenerated charge carrier separation and therefore plays a key role for efficient photochemical oxygen evolution.

1. INTRODUCTION

In the broad context of increasing energy demand and the various environmental issues related to the intensive use of fossil energy resources, water photolysis from solar light is one of the most attractive approaches to produce clean hydrogen fuel.[1] Photoelectrochemical (PEC) and powdered photocatalytic water splitting are the two main technologies which have been implemented to achieve the splitting of water into hydrogen (H_2) and oxygen (O_2) through a photocatalytic process.[2,3] First of all, in a PEC design a photoelectrode drives the reduction or oxidation reaction, while, the other charge carrier is shuttled through a wire towards another electrode which catalyzes the opposite reaction with or without light.[4,5] Conversely, particulate photocatalysts are dispersed as a colloid or anchored onto a substrate whereby photoreduction and photooxidation are catalysed by one photocatalyst or through a Z-scheme where a shuttle redox mediator transfers charge carriers between two different photocatalyts.[6-10] Whereas the photoelectrochemical method requires a sophisticated cell set-up with noble metal counter-electrodes, necessitates an external potential bias, and leads to scale-up issues, particulate photocatalysis in principle only requires a suspension of photocatalyst powders in a water basin. For instance, a thorough technoeconomic study on both designs for water splitting has shown that particulate water splitting based on baggies including particle slurries is expected to be economically viable considering 5% solar-to-H_2 conversion efficiencies and five years life-time.[11] However, particulate based systems still lag behind in efficiency.[8,10] To improve the efficiency of particulate photocatalysts to promote H_2 or O_2 evolution reactions, materials with suitable band gaps need to be combined to optimize light absorption, particle sizes need to be adapted so that diffusion length and absorption length are both accommodated and additional

contact materials should be applied to overcome intrinsic drawbacks of the main photoabsorber to create appropriate heterostructures.[6,12,13]

Bismuth vanadate ($BiVO_4$) is a non-toxic and medium band-gap (2.4 eV) n-type semiconductor which has attracted worldwide attention as a visible-light active photocatalyst.[14,15] Particularly, scheelite monoclinic $BiVO_4$ is one of the most active polymorphs in photocatalytic oxygen evolution,[16] having reached near to maximum efficiencies when implemented as a photoanode material in PEC devices.[17,18] However, the oxidation capability of bare $BiVO_4$ is hindered by weak charge carrier mobilities, short charge carrier diffusion lengths and a high charge recombination rate at the surface.[19] To circumvent these inconveniences, heterostructuring by contacting $BiVO_4$ with other materials such as TiO_2,[20] WO_3,[21,22] RuO_x[23] or (oxy)(hydr)oxides of first row transition metals (Co, Fe, Ni)[24,25] has been proposed. Thus, several studies have shown that $BiVO_4$ photoanodes modified with $NiO_x(OH)_y$ in combination with FeO_xOH_y yielded enhanced photocurrent densities in photoelectrochemical cells.[26-29] In addition, Domen *et al.* found that a 6 nm thick conformal layer of NiOOH on a $CoO_x/BiVO_4$ anode led to a threefold increase in photocurrent, reaching 2.5 mA/cm^2 at 0.6 V vs RHE.[30] On the other hand, various spinel-type Co_3O_4 or $CoO_x/BiVO_4$-based heterostructures showed enhanced photocatalytic properties for water oxidation[31] or pollutant decomposition.[32,33] The exact advantages of the first row transition metal oxides is still under debate, as some authors relate the increased water oxidation efficiencies to enhanced charge carrier separation,[34] surface passivation[35] or catalytic effects.[36]

Usually, contact materials are deposited in a random manner on particulate $BiVO_4$-based photocatalysts. In this case no distinct flow path for photogenerated holes and electrons can exist which makes bulk and surface recombination still prominent due to insufficient charge carrier

separation. Since the pioneer works of Ohno *et al.* on anatase and rutile TiO_2 particles[37] which have revealed the key role of exposed facets in the separation of photoinduced electron-hole pairs,[38,39] photodeposition is now considered as a sort of general route for synthesizing heterostructures.[40,41] Indeed, photogenerated electrons and holes preferentially accumulate on different crystalline facets which renders cocatalyst deposition regioselective depending on whether the process involves an oxidation or reduction reaction. Systematic studies on single crystalline TiO_2 (anatase) exposing different facets have shown that the different surfaces (100) vs. (110) provide indeed different electronic surface properties including different work functions which promote charge carrier separation into different directions.[42]

Anisotropic photodeposition on $BiVO_4$ microcrystals has been extensively studied by Can Li *et al.* They have first shown using field emission secondary electron microscopy (FESEM) that metallic deposits were preferentially found on {010} facets after metal ion photoreduction, while metal oxide deposits were found on the {110} facets after metal ion photo-oxidation, evidencing that electrons and holes accumulate on different sites on anisotropic $BiVO_4$ crystals.[43] Besides providing proof of enhanced charge carrier separation, the preferential photodeposition was used to construct $BiVO_4$ photocatalysts with even better photocatalytic oxygen evolution efficiencies by depositing reduction cocatalysts on the more reducing {010} facets and oxidation cocatalysts on the more oxidative {110} facets, with $Pt/BiVO_4/CoO_x$ reaching an oxygen evolution rate of 1070 $\mu mol.h^{-1}.g^{-1}$ compared to only 7 $\mu mol.h^{-1}.g^{-1}$ for bare $BiVO_4$.[44] However, the dependence of the photodeposition as a function of the cocatalyst amount has not been studied in detail in particular due to the fact of the limitations of FESEM coupled to energy dispersive X-ray spectroscopy (EDS) analyses. Moreover, even though the photodeposition of nickel based compounds has been successfully achieved onto different semiconductors such as CdS,[45] TiO_2,[46]

or even $BiVO_4$ films,[47] the regioselective deposition of nickel based oxides onto faceted $BiVO_4$ crystals has not been envisaged so far, despite the interest of this co-catalyst for photocatalytic purposes.[26,47]

We have recently reported interface experiments showing that strong upwards band bending was observed for $CoO_x/BiVO_4$ and $NiO/BiVO_4$ interfaces indicating that this kind of heterostructures should favor charge carrier separation.[34] In this context, we herein report the photodeposition of $CoO_x(OH)_y$ and $NiO_x(OH)_y$ cocatalyst, via the original use of simulated sun light, on $BiVO_4$ microcrystals exposing well-defined {010} and {110} facets. Both chemistry and regioselectivity of the deposition was investigated employing X-ray photoelectron spectroscopy and various electron microscopy techniques. Then, the photocatalytic efficiencies of the heterostructures prepared were tested for rhodamine B photodecomposition and water oxidation reactions, and were compared with previously studied $Ag/BiVO_4$ systems.

2. EXPERIMENTAL SECTION

2.1. Photocatalysts preparation

All reagents were bought in analytical grade and employed as received. Aqueous solutions were prepared using deionized water. Truncated bipyramidal $BiVO_4$ microparticles exposing well-defined facets were synthesized by optimizing and up-scaling a literature procedure.[48] The detailed synthesis procedure is described in the ESI. Cobalt (II) and nickel (II) nitrate hexahydrate ($Co(NO_3)_2.6H_2O$, $Ni(NO_3)_2.6H_2O$) and silver nitrate ($Ag(NO_3)$) were used as reagents to photo-deposit $CoO_x(OH)_y$, $NiO_x(OH)_y$, and Ag onto the microcrystalline $BiVO_4$ particles in the 0.1-10 wt% range. Sodium iodate was used as a sacrificial agent for the $CoO_x(OH)_y$ photo-deposition. A KBi buffer was used to maintain the pH at 9.2 for the $NiO_x(OH)_y$ photo-deposition.[47] It is also worth mentioning that nickel amount of about 10 wt%,

precipitation of nickel dihydroxide ($Ni(OH)_2$) was observed which has required the elimination of the precipitate before putting the solution in contact with the $BiVO_4$ microcrystals. In a typical procedure, a 100 mL aqueous solution of metal salts and additional agents was first prepared. Subsequently, 500 mg $BiVO_4$ powder was added and then sonicated for 10 min to obtain a good dispersion. The sides of the glass reaction vessel were then covered by aluminum foil so that the light source only illuminates the dispersion from the top. The suspension was then stirred during 1 h in the dark to reach adsorption equilibrium of the metal salts on the $BiVO_4$ particle surfaces. Next, the photodeposition of the metallic precursor on the $BiVO_4$ particles was initiated by switching on the solar simulator, which was used as a light source. After stirring under static air for 1-5 h, the solar simulator was switched off and the heterostructured powder was washed at least 5 times with distilled water through cycles of centrifugation and redispersion in water via sonication. Finally, drying at 70 °C for 8 h yielded about 0.45 g of the desired heterostructured photocatalyst. The precise parameters used for each system are detailed in Table S1. The solar simulator was a class AAA Newport Oriel Sol3A, using a 450 W Xenon lamp as light source, an AM 1.5G filter. It was calibrated with a certified Si-based solar cell (Newport Oriel, 91150V) to provide an incident flux of 100 $mW.cm^{-2}$ (1 sun) (Figure S1).

2.2. Photocatalysts characterization

X-ray diffractograms were recorded with a Bruker AXS diffractometer (D2 PHASER) using a Cu anode (Kα radiation). 2θ data were collected through continuous scanning from 10° to 70° with a 0.01° sampling pitch and a 6° min^{-1} scan rate. UV-Vis diffuse reflectance spectra of the powder samples were recorded using an UV-Vis-NIR spectrometer (Lambda 900) in the wavelength range of 300 to 800 nm. A JEOL JEM 2100F, equipped with a Schottky-type FEG and operated at an acceleration voltage of 200 kV, was used to perform high resolution

transmission electron microscopy (HRTEM) and energy dispersive spectroscopy (EDS). The $BiVO_4$ morphology was roughly determined through secondary electron imaging (SEI, up to 10.000X magnification) using a Hitachi TM 1000 microscope. To confirm the $BiVO_4$ morphology and analyze the spatial distribution of the metal(oxide) deposits on $BiVO_4$ high resolution secondary scanning electron microscopy (SEM) was performed with a JEOL 6700F or a JEOL 7600F, both equipped with a field emission gun and detectors for secondary electron imaging (SEI), back scattered electron imaging (BSE) and EDS. Scanning Auger microscopy (SAM) was performed with a PHI 710 scanning Auger nanoprobe, having a maximal lateral resolution of 10 nm and a maximal SEI resolution of 3 nm, to elucidate how the contact materials of the heterostructured powder samples were distributed along the particulate photoabsorbers. Different types of measuring modes were used, including point measurements (Auger spectra acquisition on a certain point), zone measurements (Auger spectra acquisition on a certain area) and mapping (Auger intensity acquisition of a certain area by scanning the area in a raster like pattern). Also SAM depth profiling, was occasionally tried, whereby an Argon ion gun (sputter rate 10 nm/min) was used to gradually sputter a sample and Auger spectra were measured after each sputter step. The oxidation state of the metal(oxide) deposits was analyzed at the DArmstadt Integrated System for MATerials research (DAISY-MAT) through X-ray photoelectron spectroscopy (XPS), using a Physical Electronics PHI 5700 multi-technique surface analysis system. XPS powder samples were prepared by applying a bit of heterostructured $BiVO_4$ powder on a thin piece of conductive indium foil placed onto a stainless steel holder. Details on the DAISY-MAT setup and handling of data are given elsewhere.[49,50]

2.3. Photocatalytic tests

Photocatalytic behaviors of the prepared photocatalysts were first evaluated by decomposition of rhodamine B (RhB, Aldrich) under simulated sun light illumination using the solar simulator described above. All experiments were performed at neutral pH, under ambient pressure and temperature. In a typical dye degradation experiment, 50 mg of the photocatalyst powder was loaded into a glass beaker together with 100 mL of a RhB aqueous solution (10 $mg.L^{-1}$ in distilled water). After sonication for 10 min to disperse the photocatalyst powder, the dispersion was stirred at 750 RPM in the dark for 30 min. At that point the shutter of the solar simulator was opened and the dispersion was illuminated. Then at time intervals of 30 min, 1.2 mL aliquots were taken from the dispersion during a period of 2 h. Next, all recuperated aliquots (normally 6 in total) were centrifuged to separate the photocatalyst powder from the RhB solution. For each aliquot, 1 mL was taken, diluted to 3 mL with distilled water, and loaded into a quartz cuvette with a 1 cm path length. The remaining RhB amount was followed by UV-visible spectroscopy monitoring the change in absorption at λ_{max} = 554 nm using a Shimadzu, UV-1650 pc spectrophotometer. Blank experiments were also conducted with catalysts in the dark and without catalysts under light irradiation. All experiments were at least repeated twice to assess the reproducibility of the experiments, and the average data for two experiments are discussed in the following. Furthermore, free radical trap experiments were conducted using a previously reported procedure (see ESI).[46]

The sacrificial photochemical water oxidation tests were carried out under an argon atmosphere with exclusion of air. Solvents were distilled under an argon atmosphere, or degassed via standard procedures prior to use and stored under argon. Each experiment was conducted in a double-walled thermostatically controlled reaction vessel (at a constant

temperature of 25 °C) which was connected via a condenser to an automatic gas burette, operated at a constant pressure (1 ± 0.05 bar). In a typical reaction, this setup was evacuated and flushed with argon three times to remove any other gases. The photocatalysts were introduced as a powder (50 mg) in the presence of sodium periodate ($NaIO_4$, 1 mmol) as sacrificial agent and using a 10 mL phosphate (10 $mmol.L^{-1}$, pH 7.0) buffered solution as reaction medium. After stirring (300 rpm) for 5 min to reach thermal equilibrium, the photochemical oxygen evolution reaction was started by illuminating the reaction vessel with a 300 W Xe lamp (LOT-QuantumDesign GmbH) with an output power of 1.5 W and equipped with a 420 nm cut-off filter. The volume of evolved gases was continuously measured by the automatic gas burette, connected to a pressure sensor. After stopping the reaction, a 1 mL gas sample was taken and analysed with a GC (Agilent GC HP 6890N) equipped with a carboxen 1000 column and a thermal conductivity detector (TCD), having argon as carrier gas. Each catalytic test ran for 20 h.

3. RESULT AND DISCUSSION

3.1 Faceted $BiVO_4$ microcrystals

Reproducible $BiVO_4$ microcrystals were synthesized using a conventional hydrothermal route by fixing the pH value at 1.5. SEM images depicted in Figure 1a indicate that the synthesized $BiVO_4$ powders exhibit truncated bipyramidal morphology. The large top faces of the microcrystals correspond to the {010} crystalline facets whereas the lateral sides can be assigned to the {110} crystalline facets. Moreover, XRD patterns reveal the formation of monoclinic scheelite $BiVO_4$ microcrystals with no signal corresponding to tetragonal $BiVO_4$ (Figure S2). These monoclinic $BiVO_4$ microcrystals were then used as substrate to photodeposit regioselectively various co-catalysts using simulated sun light.

3.2 Regioselective metal photodeposition under simulated solar light

The use of simulated sun light to achieve the photodeposition of co-catalysts onto $BiVO_4$ microcrystals was first investigated in the case of metallic silver by adapting the procedure of Li *et al.*[43] FESEM images shown in Figure S3a suggest that the silver deposition occurs on the {010} facets of the $BiVO_4$ microcrystals, whereby the size of the deposits ranges from a hundred to a few hundred nanometers. Moreover, EDS elemental maps (Figure S3b-e) show clearly well-defined silver-containing particles which therefore confirm the preparation of a heterostructured $Ag/BiVO_4$ powder. The oxidation state of the silver deposit was then closely examined by XPS (Figure S4). Only, emissions characteristic of bismuth, vanadium, silver and oxygen were detected in the survey spectrum. The line shapes of the Bi 4f and V $2p_{3/2}$ core level spectra are symmetric and the corresponding features can be attributed to Bi^{3+} and V^{5+} species.[51,52] The Ag 3d region exhibits two signals with binding energy maxima located at 368.3 eV and 374.3 eV which can be assigned to the Ag $3d_{5/2}$ and Ag $3d_{3/2}$ core levels arising from spin-orbit coupling. These energy values along with the splitting between the Ag 3d doublet, i.e. 6 eV, are consistent with the formation of metallic silver.[53,54] Those results therefore indicate that, after solar light absorption, silver cations are preferentially reduced on the {010} facets after sun light absorption probably due to the preferential accumulation of electrons onto the {010} facets as previously shown.[43,55]

3.3 Regioselective metal oxy(hydroxide) photodeposition under simulated solar light

Once the photoreduction was demonstrated, the photo-oxidation of cobalt nitrate onto $BiVO_4$ microcrystals using simulated solar light was studied. FESEM micrographs showed an increased roughness of the {110} facets which can be attributed to the regioselective deposition of cobalt-based particles (Figure 1b).[44]

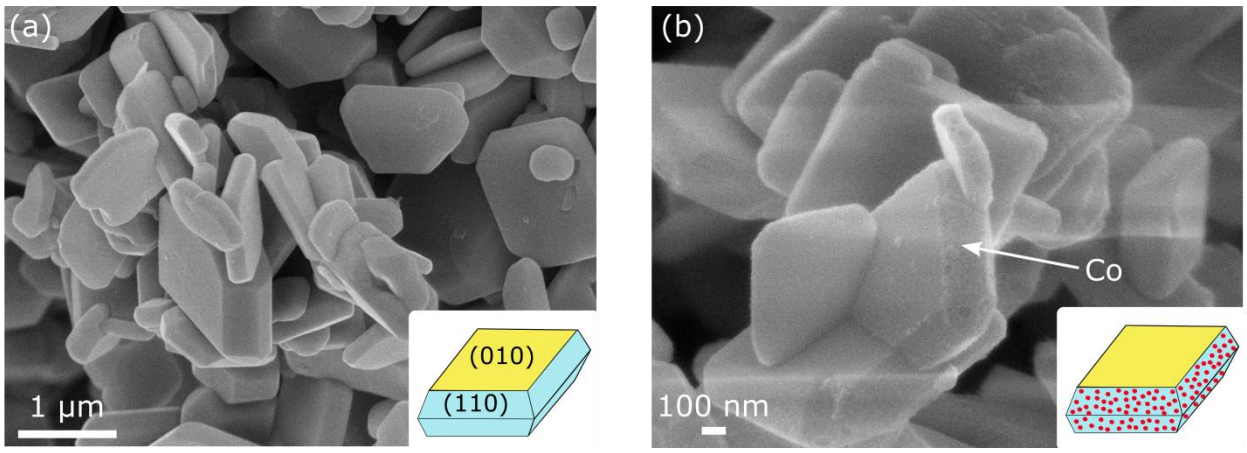

Figure 1. FESEM image of $BiVO_4$ (**a**) and 2 wt% $CoO_x(OH)_y/BiVO_4$ (**b**).

SAM mapping confirms more clearly that cobalt is almost restricted to the {110} facets while the {010} facets remain largely uncovered (Figure 2). Another important finding inferred from the SAM maps is that bismuth and vanadium signal intensity varies for the different facets. Thus, the {110} facets seem to be more bismuth rich while vanadium seems to be more abundant on the {010} facets. So far, anisotropic charge carrier mobilities[56] or higher upwards bend bending for the {110} facets[55,57] have been mainly proposed to rationalize the stronger hole accumulation on these facets. The facet specificity of the V/Bi surface stoichiometry could also play a role in the charge carrier separation. Furthermore, XPS analyses provide further insight in the oxidation state of the cobalt species. Along with the expected features for Bi^{3+} and V^{5+} species, the XPS spectra show quite complicated signals in the Co $2p_{3/2}$ region consisting of an asymmetric main line and several satellites due to plasmon loss features, electron correlations and final-state processes.[58,59] The Co $2p_{3/2}$ spectrum is similar to the one reported for CoO and $Co(OH)_2$ with a broad main line at a binding energy around 780 eV and a shoulder at 786 eV.[58,60] By contrast, the Co $2p_{3/2}$ satellite structure reported for CoOOH and Co_3O_4 species show a much smaller shoulder at 786 eV and an additional bump at a binding energy of 790 eV,[58,61] which some authors explain

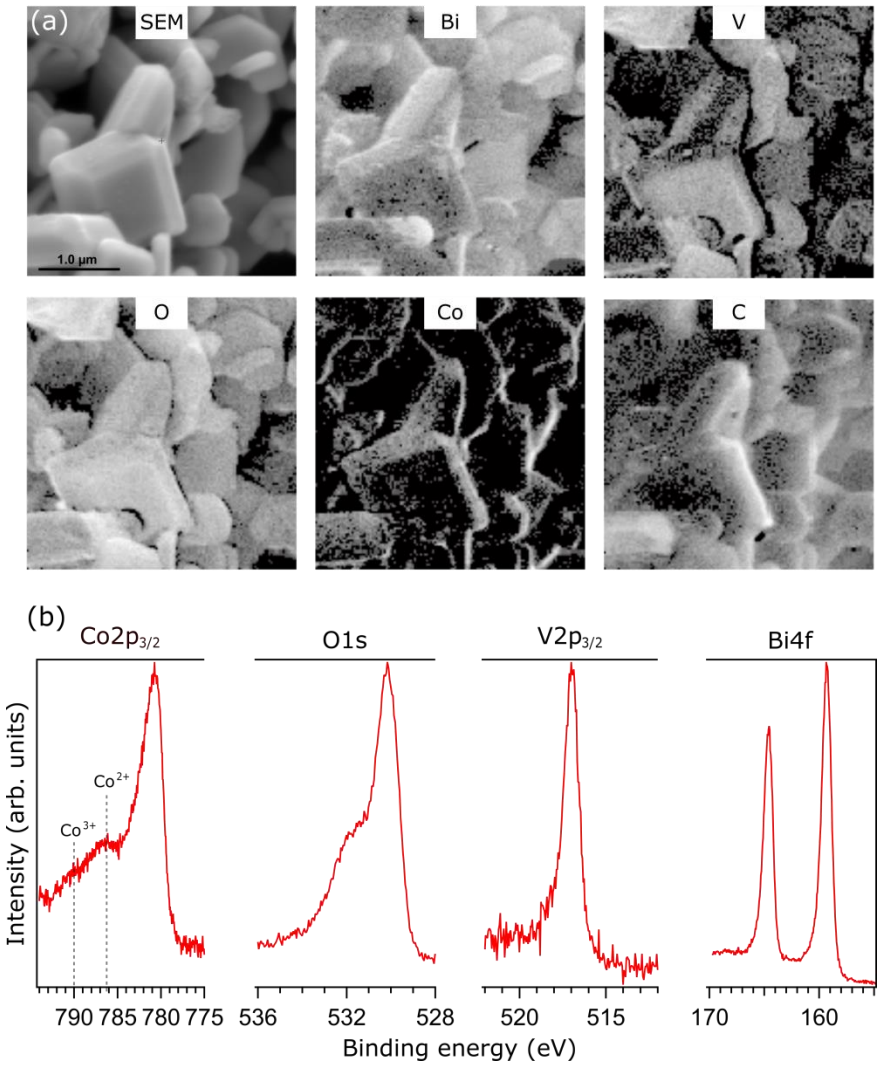

Figure 2. SAM and XPS analyses for 2 wt% $CoO_x(OH)_y/BiVO_4$. SAM elemental maps: Bi, V, O, Co and C (**a**); Core level XP spectra: $Co2p_{3/2}$, Bi4f, $V2p_{3/2}$ and O1s core level XP spectra (**b**). Dark areas in (**a**) correspond to regions where mapped element is not present.

by the (partial) cobalt oxidation state change from Co^{2+} to Co^{3+} for CoOOH and Co_3O_4.[60,62] Thus, the samples prepared in this study contain seemingly more Co^{2+}, indicating that cobalt is most likely only partly oxidized during the photodeposition process. The cobalt species should be therefore denoted as $CoO_x(OH)_y$ which is more accurate than Co_3O_4 usually proposed in the literature with similar XPS spectra.[44] At this stage, it is also worthwhile to mention that the cobalt species has been found to change during the photo-oxidation of water which makes it difficult to propose an exact composition for the cobalt co-catalyst.[60,63]

The photodeposition of nickel oxide species onto $BiVO_4$ microcrystals was then investigated for three different nominal nickel contents, i. e. 0.1, 1 and 10 wt% Ni. FESEM images suggest that the regioselectivity of the nickel-based deposit depends on the weight percentage of nickel (Figure 3). Thus, for the samples containing 1 and 10 wt% Ni, nickel seems to be unselectively deposited over the entirety of the $BiVO_4$ particle surface. This was confirmed by EDS mapping of the nickel element which showed that nickel is present on the whole surface of the $BiVO_4$ particles for the 10 wt% Ni sample (Figure 3c). By contrast, a certain regioselectivity was observed in the 0.1 wt% Ni heterostructure with a preferential nickel deposition on the edge between two {110} facets according to FESEM images (Figures 3e-f). These trends were then confirmed by SAM studies. SAM sputter profiles were run measuring the Ni L3VV Auger lines on zones corresponding to $BiVO_4$ {010} facets and {110} facets defined by SEM images (Figure g-h). An intense Ni L3VV Auger signal was detected for each zone of the microcrystals for the 1 wt% Ni sample confirming the absence of regisoselectivity for a high amount of nickel (Figure 3i). After each sputter step the Ni L3VV Auger signal intensity decreases, confirming that Ni is predominantly located at the $BiVO_4$ particle surface. Contrarily, for the 0.1 wt% Ni sample a Ni L3VV Auger signal is only visible when zones on the {010} facets were measured (Figure 3j). In addition, bright-field and dark-field STEM images on the edge of the {110} facets for the 0.1 wt% Ni sample reveal the presence of small particles which can be attributed to nickel oxide species according to EDS analyses (Figure S5). As a consequence, the nickel deposit appears to be limited to the {010} facets and the edges between the {110} facets in the 0.1 wt% Ni heterostructure.

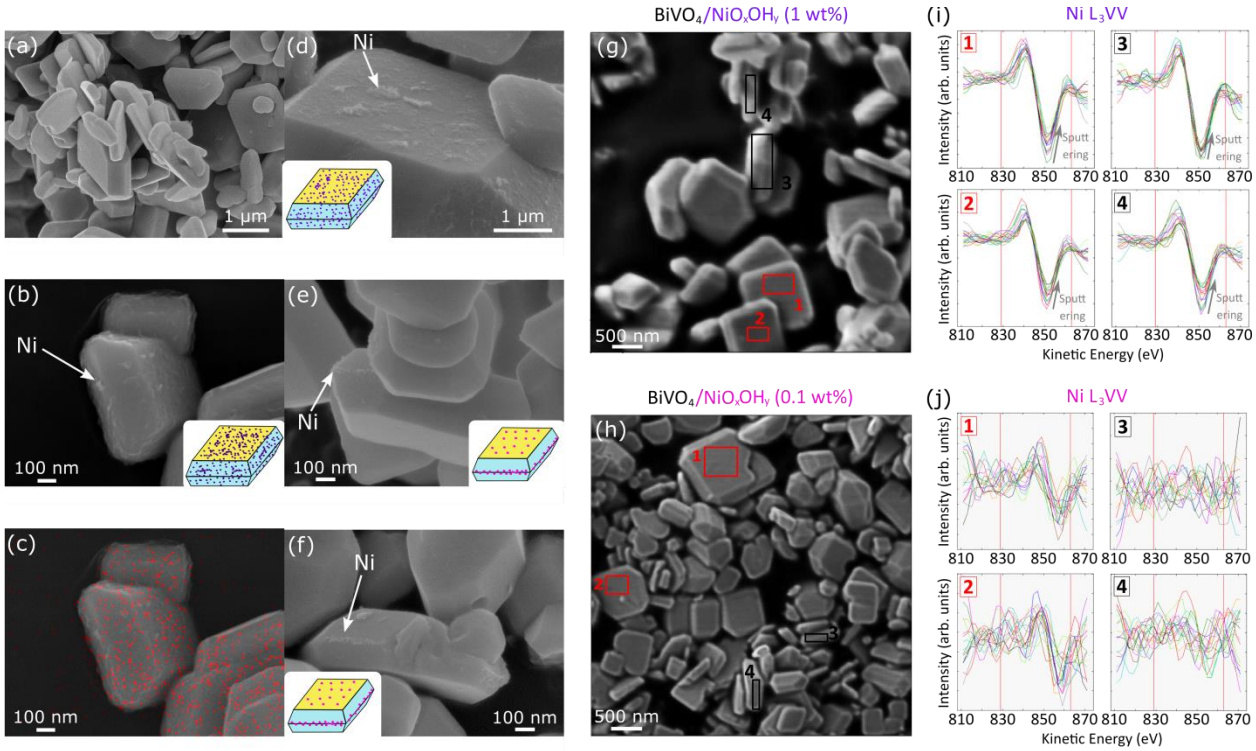

Figure 3. SEM images for bare $BiVO_4$ (**a**), 10 wt% $NiO_x(OH)_y/BiVO_4$ (**b**), 10 wt% $NiO_x(OH)_y/BiVO_4$ with Ni EDS mapping (**c**), 1 wt% $NiO_x(OH)_y/BiVO_4$ (**d**) and 0.1 wt% $NiO_x(OH)_y/BiVO_4$ (**e-f**). SEM images for 1 wt% $NiO_x(OH)_y/BiVO_4$ (**g**) and 0.1 wt% $NiO_x(OH)_y/BiVO_4$ (**h**) indicating on which zones Ni L_3VV SAM sputter profiles were measured. Ni L_3VV SAM sputter profiles for 1 wt% $NiO_x(OH)_y/BiVO_4$ (**i**) and 0.1 wt% $NiO_x(OH)_y/BiVO_4$ (**j**) Areas 1 and 2 correspond to {110} facets while areas 3 and 4 stands for {010} facets.

Further insights in the surface composition of the 0.1 wt% and 1 wt% Ni samples were inferred from XP core level spectra of Ni 2p, O 1s, V $2p_{3/2}$ and Bi 4f (Figure 4). As for the other heterostructures, the core level binding energies found for V $2p_{3/2}$ and Bi 4f are characteristic of V^{5+} and Bi^{3+} chemical states in $BiVO_4$.[51,52] As expected, the Ni 2p-to-Bi 4f intensity ratio is higher for the 1 wt% Ni sample compared to the 0.1 wt% Ni one. Furthermore, two main features are detected in the O 1s core level spectrum at 530.3 eV and 532.2 eV, respectively. The former can be assigned to metal oxides, i.e. O^{2-} sites, while the latter is typical for hydroxyl groups and organic carbon-oxygen bonds, commonly present in ex situ prepared samples due to adherence of water and organic compounds onto the sample surface.[52] It is also worth underlining that the

hydroxyl feature is considerably more intense than usual, even higher than the O^{2-} signal, for the 1 wt% Ni sample which suggests a large amount of hydroxide species. Finally, the Ni 2p core level region is complex with four main features at 856.6 eV belonging to Ni $2p_{3/2}$, 861.5 eV belonging to a Ni $2p_{3/2}$ satellite, 874.3 eV belonging to Ni $2p_{1/2}$ and 880.7 eV corresponding to a Ni $2p_{1/2}$ satellite. The presence of pure NiO and metallic nickel can be excluded, since that would give rise to a noticeable peak splitting of the main Ni 2p3/2 line at 856.5 eV for NiO[64] and a characteristic Ni 2p3/2 feature at 852.6 eV for Ni[65] which are not observed here. Instead, the Ni 2p line shape resembles more to that reported for a mixed nickel oxyhydroxide.[64,66] As a result, the nickel species should be designated as $NiO_x(OH)_y$.

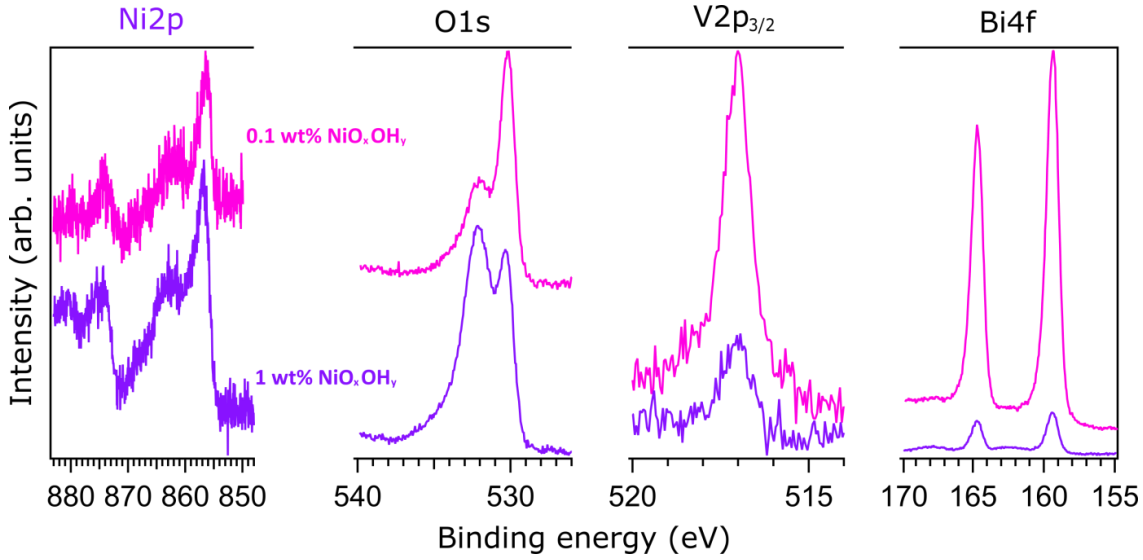

Figure 4. Core level XP spectra for 0.1 wt% and 1 wt% $NiO_x(OH)_y/BiVO_4$: Ni 2p (**a**), O 1s (**b**), V $2p_{3/2}$ (**c**) and Bi 4f (**d**) core level XP spectra.

3.4 Photocatalytic properties

First of all, the optical band gaps of the different heterostructures prepared were determined by UV-visible diffuse reflectance spectroscopy (Figure S6a). It is generally admitted that $BiVO_4$ is an indirect band gap semiconductor,[67] whereas light absorption involves direct transition. Thus, Tauc plots of $[F(R)h\nu]^2$ vs. hν led to direct optical band gap in the range of 2.48-2.52 eV while

Tauc plots of $[F(R)h\nu]^{1/2}$ vs. hν yielded indirect optical band gap of about 2.41-2.43 eV (Figure S6b-c). This shows that the deposited contact materials do not have a strong influence on the light absorption properties of the heterophotocatalysts.

The photocatalytic properties were first examined by the photodecomposition of RhB over different photocatalysts (with a co-catalyst loading of 0.1 wt%) under simulated sun light (1 sun) and static air (Figure S7). A blank experiment in the absence of photocatalyst confirms that photolysis of RhB under sun light can be neglected. Thus, 0.1 wt% $Ag/BiVO_4$ and 0.1 wt% $NiO_x(OH)_y/BiVO_4$ photocatalysts appeared to be the most efficient with about 50% dye decomposition after 2h irradiation while 0.1 wt% $CoO_x(OH)_y/BiVO_4$ showed a lower activity, similar to that of bare $BiVO_4$. Photodegradation of RhB by these materials can be modeled by using a pseudo first order kinetic law, $\ln(C/C_0) = k_{app}t$ where k_{app} is the pseudo first-order rate constant and, C and C_0 stand for the concentration of the dye in solution at time t and 0. Apparent rate constants were estimated to be 3.3 10^{-3} min^{-1}, 2.7 10^{-3} min^{-1}, 5.5 10^{-3} min^{-1} and 6.7 10^{-3} min^{-1} for $BiVO_4$, 0.1 wt% $CoO_x(OH)_y/BiVO_4$, 0.1 wt% $NiO_x(OH)_y/BiVO_4$ and 0.1 wt% $Ag/BiVO_4$, respectively. While the beneficial effect of metallic silver particles in $BiVO_4$ based photocatalysis is well-documented,[68,69] it is the first time that the same trend is reported for $NiO_x(OH)_y$ deposits. For $Ag/BiVO_4$ system, it has been reported that superoxide radicals ($O_2^{\bullet -}$) are the main species involved in the degradation of organics.[69] To get an insight in the radicals involved in the case of the original 0.1 wt% $NiO_x(OH)_y/BiVO_4$ photocatalyst, propan-2-ol (IPA), 1,4-benzoquinone (BQ) and potassium iodide (KI) were used as hydroxyl radical ($OH^{\bullet}$), superoxide radical ($O_2^{\bullet -}$) and hole (h^+) scavengers, respectively for RhB photodecomposition. Figure S8 reports on the kinetic rate constant found in each case normalized by that in the absence of trapping agents. Thus, addition of IPA and KI has strongly diminished the

photocatalytic activity of 0.1 wt% $NiO_x(OH)_y/BiVO_4$ material while BQ led to a less pronounced decrease. As a result, $O_2^{\bullet-}$ radicals which are only formed by photogenerated electrons are not the dominant species ruling the photocatalytic activity while holes play an important role in the photocatalytic decomposition of RhB in the presence of the $NiO_x(OH)_y/BiVO_4$ system. This could be due to the combination of a catalytic effect of $NiO_x(OH)_y$ particles lowering the activation energy with an enhanced hole collection at the $NiO_x(OH)_y$-$BiVO_4${110} interface.

Then, photochemical sacrificial water splitting experiments were carried out to determine the ability of the different photocatalysts to promote O_2 evolution reaction in the presence of an electron scavenger (sodium periodate). At this stage, it is worth mentioning that the use of sacrificial reagents may lead to undesired phenomena such as side reactions, deactivation and changing driving forces.[70] Nonetheless, this approach allows for a simplification of the complex system of overall water splitting and hence a more detailed understanding of the basic processes. As depicted in Fig. 5A, no significant amount of O_2 was generated in the absence of light while a volume increase of 1 mL was observed for a blank experiment without photocatalyst (Fig. S9). In contrast irradiation for 6 h of 0.2 wt% $CoO_x(OH)_y/BiVO_4$ suspensions in $NaIO_4$/water mixture led to the production of about 12 mL of O_2 evidencing the occurrence of an actual photocatalytic process. Typical plots of the time course of O_2 evolution for the different photocatalysts investigated are shown in Fig. 5B. Regardless of the photocatalyst nature, the amount of evolved O_2 was increasing linearly with time thus revealing the high stability of the photocatalysts to reach a plateau value which corresponds to the total consumption of the scavenger (see ESI). This result evidences that reduction of IO_4^- does not constitute the rate-limiting step.

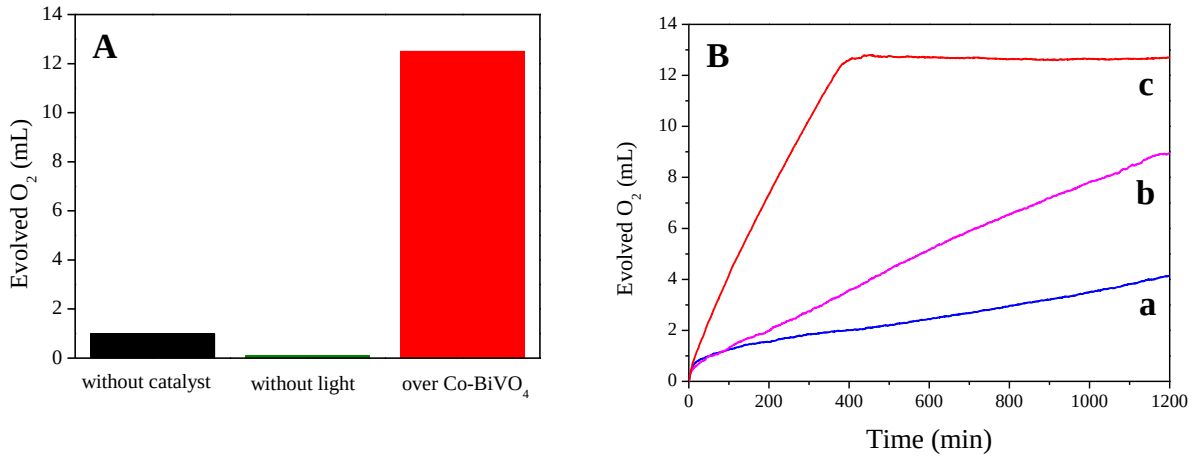

Figure 5. (**A**) Photocatalytic evolution of O_2 under different conditions. (**B**) O_2 evolution over bare $BiVO_4$ (a, blue), 1 wt% $NiO_x(OH)_y/BiVO_4$ (b, magenta) and 0.2 wt% $CoO_x(OH)_y/BiVO_4$ (c, red).

To get a more quantitative insight in the photocatalytic properties, a linear regression was performed on the linear part of the gas evolution curves, i.e. at a reaction time between 2 and 3 h, and the resulting rates are gathered in Table 1. Implementation of $CoO_x(OH)_y$ as co-catalyst boosts the sacrificial water oxidation performance of $BiVO_4$ by about 10 times, with respect to bare $BiVO_4$. However, the $NiO_x(OH)_y/BiVO_4$ heterostructures exhibited only a fair water oxidation rate compared to the other heterostructures, since the O_2 evolution is only twice as high with respect to bare $BiVO_4$. These results may be related to the highly regioselective deposition of the $CoO_x(OH)_y$ oxidation co-catalyst on the electron-deficient {110} facets of $BiVO_4$ microcrystals compared to $NiO_x(OH)_y$ which is mainly located on the electron-rich {010} facets of $BiVO_4$. The $CoO_x(OH)_y$ regioselectivity, the preferential accumulation of holes on the {110} facets[44,55] and upwards band bending at $CoO_x/BiVO_4$ contacts[34] favors the spatial charge separation of the photogenerated charge carriers which inhibits charge recombination and leads to enhanced photocatalytic O_2 evolution rate.

Table 1: O_2 evolution rates of some photocatalysts prepared in this work in comparison with those reported in literature for state of the art photocatalysts based on $BiVO_4$. All the literature data have been acquired under visible light ($\lambda > 420$ nm) using a 300 W Xe lamp.

Photocatalyst	Electron scavenger	O_2 evolution ($\mu mol.h^{-1}.g^{-1}$)	Ref
$BiVO_4$	0.1 M $NaIO_4$	154	This work
0.1 wt% $NiO_x(OH)_y$ /$BiVO_4$	0.1 M $NaIO_4$	292	This work
1 wt% $NiO_x(OH)_y$ /$BiVO_4$	0.1 M $NaIO_4$	304	This work
0.08 wt% $CoO_x(OH)_y$/$BiVO_4$	0.1 M $NaIO_4$	1330	This work
0.2 wt% $CoO_x(OH)_y$/$BiVO_4$	0.1 M $NaIO_4$	1538	This work
$BiVO_4$	0.05 M $AgNO_3$	835	14
$BiVO_4$	0.05 M $AgNO_3$	920	72
PO_4-doped $BiVO_4$	aqueous $AgNO_3$	670	73
S-doped-C_3N_4/$BiVO_4$	0.05 M $AgNO_3$	750	74
Ru-$SrTiO_3$:Rh-RGO/$BiVO_4$	H_2SO_4	167	75
Ru-$SrTiO_3$:Rh/$BiVO_4$	H_2SO_4	540	76
Pt/$BiVO_4$/MnO_x	0.02M $NaIO_3$	630	43
Pt/$BiVO_4$/Co_3O_4	0.02M $NaIO_3$	1070	44
V_o-ZnO/$BiVO_4$	0.05 M $AgNO_3$	1356	77

3.5 Discussion

The photodeposition of various co-catalysts onto faceted $BiVO_4$ microcrystals has been successfully achieved using 1 sun illumination with a regioselectivity strongly dependent upon the co-catalyst used. The expected facet-selectivity was actually observed for both silver and cobalt photodeposition carried out at pH 7.[43,44] Under these pH conditions, the main metallic precursor species are cationic, i.e. Ag^+ or Co^{2+}, and $BiVO_4$ truncated bipyramidal surfaces are

negatively charged since the isoelectric point of these microparticles has been reported to be about 3.5.[43] As a consequence, specific adsorption of the metallic precursor cannot be at the origin in the difference of the regioselectivity observed. On the other hand, as the same counter-ion, i.e. NO_3^-, was used in both cases, preferential chemisorption of anions on specific facets can be ruled out to interpret the facet selectivity. Finally, favored interactions of the neutral, i.e. methanol, or negatively charged, i.e. IO_3^-, hole or electron scavengers with specific facets is unlikely owing to the negative charge of the $BiVO_4$ surfaces. The regioselectivity for the Ag and $CoO_x(OH)_y$ deposition can therefore be assigned to the different electrochemical properties of the {010} and {110} facets under light irradiation which favors the reduction of silver cations on the electron-rich {010} facets and the oxidation of the cobalt precursor on the electron-deficient {110} facets of the $BiVO_4$ microcrystals. These findings obtained at 1 sun are fully consistent with those previously reported with other light sources.[43,44]

On the other hand, the regioselectivity of the nickel photodeposition strongly depends on the wt% of nickel in the reaction mixture since nickel species was selectively deposited onto the {010} facets and the edges between the {110} facets in the 0.1 wt% $NiO_x(OH)_y/BiVO_4$ sample whereas no selectivity was detected for nickel amount equal to or higher than 1 wt%. Overall, the difference in regioselectivity of Co and Ni is striking due to their very similar chemistry. The standard oxidation potentials for the oxidation of Co^{2+} to CoOOH (1.76 V) and Ni^{2+} to NiOOH (2.05 V) are close and both allowed according to the $BiVO_4$ VBM of about 2.8 V vs NHE. Similarly, the standard reduction potentials for the reduction of Co^{2+} to Co(s) (-0.282 V) and Ni^{2+} to Ni(s) (-0.236 V) can thermodynamically not take place at the $BiVO_4$ surface under light illumination, because of the more positive $BiVO_4$ CBM.[71] Thus, only oxidation of Ni^{2+} is assumed just as for Co^{2+}. The difference in regioselectivity could have to do with the difference

in pH, as Co^{2+} was deposited at pH 7, while Ni^{2+} was deposited at pH 9.2 using a KBi buffer. The {010} facets could be more negatively charged, leading to a preferential adsorption of the Ni^{2+} ions onto these facets. The Ni^{2+} ions could then react with OH^- leading to an impregnation onto the {010} facets. Regarding the suitable standard reduction potential (0.52 V) the impregnated $Ni(OH)_2$ could then further oxidize to NiOOH during light illumination.[71] Additionally, the regioselective adsorption of Ni on the {110} edges could be due to even higher hole accumulation on these edges than on the {110} facets, so that for low Ni^{2+} concentrations only photodeposition takes place on the{110} edges.

As far as the photocatalytic properties are concerned, the rates found for the photodecomposition of RhB in the presence of 0.1 wt% $NiO_x(OH)_y/BiVO_4$ and 0.1 wt% $Ag/BiVO_4$ under static air fall within the range of those reported by Li *et al.* for $BiVO_4$ microcrystals endowed with a single co-catalyst under oxygen bubbling.[44] As a result, associated with $BiVO_4$ particles, $NiO_x(OH)_y$ is a good co-catalyst for the photodegradation of organics. Moreover, comparison with literature indicates that the materials developed in this study compete well with the most efficient photocatalysts for sacrificial water oxidation reaction (Table 1).[14,43,44,72-77] First of all, our results are on line with those reported by Li *et al.* for similar morphologies,[44] in the sense that boosted water oxidation performances were obtained for cobalt based materials. In addition, the O_2 evolution reaction rates for $BiVO_4$, 0.1 wt% $NiO_x(OH)_y/BiVO_4$ and 0.2 wt% $CoO_x(OH)_y/BiVO_4$ were significantly higher than those described by Li *et al.* for $BiVO_4$, $Co_3O_4/BiVO_4$ and $Pt/BiVO_4$, i.e. 6.7, 16.7 and 112.0 $\mu mol.h^{-1}.g^{-1}$.[44] These data reveal the quality of the faceted $BiVO_4$ microcrystals and the cobalt oxide deposit obtained under sun light illumination. Finally, the overview provided in Table 1 clearly indicates that the 0.2 wt% $CoO_x(OH)_y/BiVO_4$ led to one of the highest sacrificial O_2 evolution

rate ever reported in the literature. Figure 6 depicts the band alignment of our $CoO_x(OH)_y/BiVO_4$ and $NiO_x(OH)_y/BiVO_4$ heterostructured particles along the [010] and [110] direction based on the differences in band alignment along the [010] and [110] direction for bare truncated bipyramidal $BiVO_4$ crystals,[55] the band alignment at the $CoO_x/BiVO_4$ and $NiO/BiVO_4$ contacts[34] and the observed regioselectivity. Surface photovoltage measurements on truncated bipyramidal $BiVO_4$ crystals have demonstrated upwards band bending in the [110] direction, which is almost absent in the [010] direction.[55] For both $CoO_x/BiVO_4$ and $NiO/BiVO_4$ strong upwards band bending at the heterocontact in $BiVO_4$ has been observed.[34] Because Co cocatalyst could only be detected on the [110] facets of $CoO_x(OH)_y/BiVO_4$ upwards band bending can be expected in the [110] direction but not in the [010] direction. As a consequence of the upward band bending in the [110] direction holes will be driven to the $CoO_x(OH)_y$ coated [110] facets, whereas the electrons will move to the {010} facets with no/small band bending. This clear and strong difference in band bending along the different crystalline directions allow for clear charge carrier separation and reduced surface charge carrier recombination and could explain why a remarkable water oxidation efficiency was reached with $CoO_x(OH)_y/BiVO_4$. In contrast, Ni cocatalyst could be found on the edges of the {110} facets and on the {010} facets. Therefore, upwards band bending can be expected in the [110] direction and the [010] direction, giving no clear separation path for light induced electron-hole pairs. Another reason why our heterostructured $BiVO_4$ photocatalysts exhibited a better water oxidation efficiency than bare $BiVO_4$ could be due to enhanced surface passivation, since Zachäus *et al.* showed using intensity modulated photocurrent spectroscopy that CoPi effectively passivated the surface of $BiVO_4$.[35] For a more detailed analysis on the relative contributions of the suggested mechanistic explanations single

crystalline studies with well defined surface facets would be of interest as have been performed on anatase TiO_2.[42]

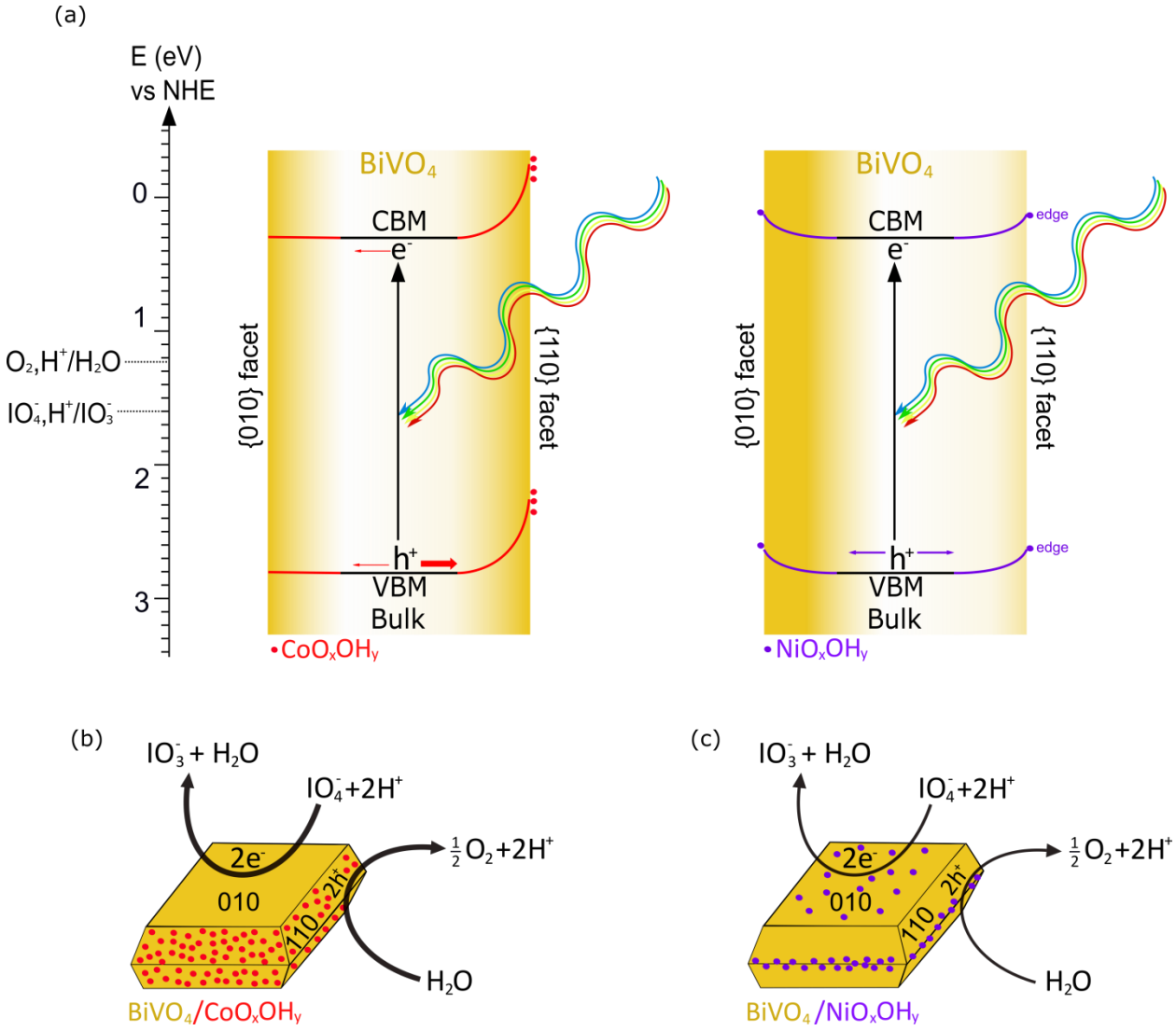

Figure 6. Schematic of the energy band alignment for $CoO_x(OH)_y/BiVO_4$ and $NiO_x(OH)_y/BiVO_4$ along the [010] and [110] direction, showing the potential pathways of light induced charge carriers (**a**). Schematics of the electrochemical sacrificial oxygen evolution reactions on $CoO_x(OH)_y/BiVO_4$ and $NiO_x(OH)_y/BiVO_4$ using $NaIO_4$ as sacrificial agent. The thickness of the arrows corresponds to the efficiency of the reactions.

4. CONCLUSION

In this work, we have demonstrated that $Ag/BiVO_4$, $CoO_x(OH)_y/BiVO_4$ and new $NiO_x(OH)_y/BiVO_4$ heterostructures could be successfully synthesized through an original sun light photodeposition route. Combining scanning electron and Auger microscopy with X-ray photoelectron spectroscopy enabled to unravel the regioselectivity and the chemical nature of the co-catalyst deposits. Metallic silver (Ag) and cobalt (oxy)hydroxide ($CoO_x(OH)_y$) particles were selectively deposited onto the {010} and {110} facets, respectively, of {010}/{110} dual facet exposed $BiVO_4$ microcrystals. On the other hand, nickel (oxy)hydroxide ($NiO_x(OH)_y$) photodeposition shows no facet selectivity for nickel precursor amount higher than 1 wt% while an original selectivity was observed for 0.1 wt% $NiO_x(OH)_y/BiVO_4$ with a preferential deposition onto the {010} facets and the edges between the {110} facets. In addition, most of the heterostructures prepared showed enhanced photocatalytic properties. Thus, 0.1 wt% $Ag/BiVO_4$, and 0.1 wt% $NiO_x(OH)_y/BiVO_4$ led to almost twice higher decomposition rates of RhB than bare $BiVO_4$ under simulated sun illumination. More interestingly, for sacrificial water oxidation 0.2 wt% $CoO_x(OH)_y/BiVO_4$ yielded one of the highest oxygen evolution rates, i.e. 1538 $\mu mol.h^{-1}.g^{-1}$, ever reported in the literature which represents a tenfold increase compared to bare $BiVO_4$. Our study therefore emphasizes the key contribution of regioselective deposition of cobalt oxide species onto the more electron-deficient facet of truncated bipyramidal scheelite $BiVO_4$ microcrystals for efficient oxygen evolution reaction. Finally, this work shed light on the potentialities of solar irradiation instead of conventional lamps to fabricate efficient heterostructured photocatalysts by associating an appropriate co-catalyst and selective deposition onto the specific facet of metal oxide photoabsorbers. The results obtained in our study support the idea to fabricate well defined heterostructures of absorber materials coupled to co-catalysts

working as contact and catalytic center. A challenging but rewardable research direction of nanotechnology would be to form facetted nanocrystals with electronically well defined facets for electron and hole scavenging, the effect of which will be supported by cocatalyst materials with strongly deviating electronic properties. In short, a nano-sized cell arrangement with contact materials providing an adapted electronic contact, but also preferential catalytic properties would be favorable.

ASSOCIATED CONTENT

Supporting Information. XRD patterns, UV-visible spectroscopy data, complementary SEM, SAM and XPS data, RhB photodecomposition data.

AUTHOR INFORMATION

Corresponding Author

* Corresponding author at : Université de Bordeaux, Institut des Sciences Moléculaires, ISM UMR 5255 CNRS, 351 Cours de la Libération, F-33405 Talence Cédex, France.

E-mail address: thierry.toupance@u-bordeaux.fr

Author Contributions

The manuscript was written through contributions of all authors.

ACKNOWLEDGMENT

The researches described in this manuscript were performed in the framework of ITN-EJD-FunMat (European Joint Doctorate for Multifunctional Materials) and was supported by the

European Union's Horizon 2020 research and innovation program through the Marie Sklodowska-Curie Grant Agreement No 641640. The authors acknowledge the "Université Franco-allemande" for funding the German-French Doctoral College in Functional Materials (contract CDFA 02-15 (2018-2021)). The PLACAMAT structure for its electron microscopy facilities and EMMI (European Multifunctional Material Institute) are also thanked.

REFERENCES

(1) van de Krol, R.; Parkinson, B. A. Perspectives on the Photoelectrochemical Storage of Solar Energy. *MRS Energy Sustain.* **2017**, *4*, E13.

(2) Ardo, S.; Ardo, S.; Rivas, D. F.; Modestino, M. A.; Greiving, V. S.; Abdi, F. F.; Llado, E. A.; Artero, V.; Ayers, K.; Battaglia, C.; Becker, J.-P.; Bederak, D.; Berger, A.; Buda, F.; Chinello, E.; Dam, B.; Di Palma, V.; Edvinsson, T. ; Fujii, K.; Gardeniers, H.; Geerlings, H.; Hashemi, S. M. H.; Haussener, S.; Houle, F.; Huskens, J.; James, B. D.; Konrad, K.; Kudo, A.; Kunturu, P. P.; Lohse, D.; Mei, B.; Miller, E. L.; Moore, G. F.; Muller, J.; Orchard, K. L.; Rosser, T. E.; Saadi, F. H.; Schüttauf, J.-W.; Seger,B.; Sheehan, S. W.; Smith, W. A. Spurgeon, J.; Tang, M. H.; van de Krol, R.; Vesborg, P. C. K.; Westerik, P. Pathways to Electrochemical Solar-Hydrogen Technologies. *Ener. Environ. Sci.* **2018**, *11*, 2768–2783.

(3) Ahmed, M; Dincer, I. A Review on Photoelectrochemical Hydrogen Production Systems: Challenge and Future Directions. *Int. J. Hydrogen Ener.* **2019**, *44*, 2474–2507.

(4) Sivula, K.; van de Krol, R. Semiconducting Materials for Photoelectrochemical Energy Conversion. *Nat. Rev. Mater.* **2016**, *1*, 15010.

(5) Jiang, C; Moniz, S. J. A.; Wang, A.; Zhang, T.; Tang, J. Photoelectrochemical Devices for Solar Water Splitting – Materials and Challenges. *Chem. Soc. Rev.* **2017**, *46*, 4645–4660.

(6) Kudo, A.; Miseki, Y. Heterogeneous Photocatalyst Materials for Water Splitting. *Chem. Soc. Rev.* **2009**, *38*, 253–278.

(7) Maeda, K. Z-Scheme Water Splitting Using Two Different Semiconductor Photocatalysts. *ACS Catal.* **2013**, *3*, 1486–1503.

(8) Wang, Q.; Hisatomi, T.; Jia, Q.; Tokudome, H.; Zhong, M.; Wang, C.; Pan, Z.; Takata, T.; Nakabayashi, M.; Shibata, N.; Li, Y.; Sharp, I. D.; Kudo, A.; Yamada, T. Domen, K. Scalable Water Splitting on Particulate Photocatalyst Sheets with a Solar-to-Hydrogen Energy Conversion Efficiency Exceeding 1%. *Nat. Mater.* **2016**, *15*, 611–615.

(9) Wang, Q.; Hisatomi, T.; Suzuki, Y.; J Pan, Z.; Seo, J.; Katayama, M.; Minegishi, T.; Nishiyama, H.; Takata, T.; Seki, K.; Kudo, A.; Yamada, T. Domen, K. Particulate Photocatalyst Sheets Based on Carbon Conductor Layer for Efficient Z-Scheme Pure-Water Splitting at Ambient Pressure. *J. Am. Chem. Soc.* **2017**, *139*, 1675–1683.

(10) Goto, Y.; Hisatomi, T.; Wang, Q.; Higashi, T.; Ishikiriyama, K.; Maeda, T.; Sakata, Y.; Okunada, S.; Tokudome, H.; Katayama, M.; Akiyama, S.; Nishiyama, H.; Inoue, Y.; Takewaki, T.; Setoyama, T.; Minegishi, T.; Takata, T.; Yamada, T. Domen, K. Particulate Photocatalyst Sheets Based on Cabon Conductor Layer for Efficient Z-Scheme Pure-Water Splitting at Ambient Pressure. *Joule* **2018**, *2*, 509–520.

(11) Pinaud, B. A.; Benck, J. D.; Seitz, L. C.; Forman, A. J.; Chen, Z.; Deutsch, T. G.; James, B. D.; Baum, K. N.; Baum, G. N.; Ardo, S.; Wang, H.; Miller, E.; Jaramillo, T. F. Technical and

Economic Feasibility of Centralized Facilities for Solar Hydrogen Production via Photocatalysis and Photoelectrochemistry. *Ener. Environ. Sci.* **2013**, *6*, 1983–2002.

(12) Hanna, M. C.; Nozik, A. J. Solar Conversion Efficiency of Photovoltaic and Photoelectrolysis Cells with Carrier Multiplication Absorbers. *J. Appl. Phys.* **2006**, *100*, 74510.

(13) Osterloh, F. E. Inorganic Nanostructures for Photoelectrochemical and Photocatalytic Water Splitting. *Chem. Soc. Rev.* **2013**, *42*, 2294–2320.

(14) Yu, J.; Kudo, A. Effects of Structural Variation on the Photocatalytic Performance of Hydrothermally Synthesized $BiVO_4$. *Adv. Func. Mater.* **2006**, 16, 2163–2169.

(15) Malathi, A.; Madhavan, J.; Ashokkumar, M.; Arunachalam, P. A Review on $BiVO_4$ Photocatalyst : Activity Enhancement Methods for Solar Photocatalytic Applications. *Applied Catal. A, General* **2018**, *555*, 47–74.

(16) Kudo, A.; Omori, K.; Kato, H. A Novel Aqueous Process for Preparation of Crystal Form-Controlled and Highly Crystalline $BiVO_4$ Powder from Layered Vanadates at Room Temperature and Its Photocatalytic and Photophysical Properties. *J. Am. Chem. Soc.* **1999**, *121*, 11459–11467.

(17) Abdi, F. F.; Han, L. ; Smets, A. H. M.; Zeman, M.; Dam, B. ; van de Krol, R. Efficient Solar Water Splitting by Enhanced Charge Separation in a Bismuth Vanadate-silicon Tandem Photoelectrode. *Nat. Commun.* **2013**, *4*, 17594–17598.

(18) Sharp, I. D.; Cooper, J. K.; Toma, F. M.; Buonsanti, R. Bismuth Vanadate as a Platform for Accelerating Discovery and Development of Complex Transition-Metal Oxide Photoanodes. *ACS Energy Lett.* **2017**, *2*, 139–150.

(19) Cho, S. K.; Park, H. S.; Lee, H. C.; Nam, K. M.; Bard, A. J. Metal Doping of $BiVO_4$ by Composite Electrodeposition with Improved Photoelectrochemical Water Oxidation. *J. Phys. Chem. C*, **2013**, *117*, 23048–23056.

(20) Zalfani, M.; van der Schueren, B.; Hu, Z.-Y.; Rooke, J. C.; Bourguiga, R.; Wu, M.; Van Tendeloo, G.; Su, B.-L. Novel 3DOM $BiVO_4/TiO_2$ Nanocomposites for Highly Enhanced Photocatalytic Activity. *J. Mater. Chem. A* **2015**, *3*, 21244–21256.

(21) Pihosh, Y.; Turkevych, I.; Mawatari, K.; Uemura, J.; Kazoe, Y.; Kosar, S.; Makita, K.; Sugaya, T.; Matsui, T.; Fujita, D.; Tosa, M.; Kondo, M.; Kitamori, T. Photocatalytic Generation of Hydrogen by Core-shell $WO_3/BiVO_4$ Nanorods with Ultimate Water Splitting Efficiency. *Sci. Rep.* **2015**, *5*, 11141.

(22) Xia, L.; Bai, J.; Li, J.; Zeng, Q.; Li, X.; Zhou, B. A Highly Efficient $BiVO_4/WO_3/W$ Heterojunction Photoanode for Visible-light Responsive Dual Photoelectrode Photocatalytic Fuel Cell. *Appl. Catal. B: Environ.* **2016**, *183*, 224–230.

(23) Lin, F.; Wang, D.; Jiang, Z.; Ma, Y.; Li, J.; Li, R.; Li, C. Photocatalytic Oxidation of Thiophene on $BiVO_4$ with Dual Co-catalysts Pt and RuO_2 Under Visible Light Irradiation Using Molecular Oxygen as Oxidant. *Ener. Environ. Sci.* **2012**, *5*, 6400–6406.

(24) Ye, H.; Park, H. S.; Bard, A. J. Screening of Electrocatalysts for Photoelectrochemical Water Oxidation on W-Doped $BiVO_4$ Photocatalysts by Scanning Electrochemical Microscopy. *J. Phys. Chem. C* **2011**, *115*, 12464–12470.

(25) McCrory, C. C. L.; Jung, S.; Peters, J. C.; Jaramillo, T. F. Benchmarking Heterogeneous Electrocatalysts for the Oxygen Evolution Reaction. *J. Am. Chem. Soc.* **2013**, *135*, 16977–16987.

(26) Kim, T. W.; Choi, K.-S. Nanoporous $BiVO_4$ Photoanodes with Dual-Layer Oxygen Evolution Catalysts for Solar Water Splitting. *Science* **2014**, *343*, 990–994.

(27) Qiu, Y.; Liu, W.; Chen, W.; Chen, W.; Zhou, G.; Hsu, P.-C.; Zhang, R.; Liang, Z.; Fan, S.; Zhang, Y.; Cui, Y. Efficient Solar-driven Water Splitting by Nanocone $BiVO_4$-perovskite Tandem Cells. *Sci. Adv.* **2016**, *2*, e1501764.

(28) Shi, X.; Choi, I. Y.; Zhang, K.; Kwon, J.; Kim, D. Y.; Lee, J. K.; Oh, S. H.; Kim, J. K.; Park, J. H. Efficient Photoelectrochemical Hydrogen Production from Bismuth Vanadate-decorated Tungsten Trioxide Helix Nanostructures. *Nat. Commun.* **2014**, *5*, 4775.

(29) Shi, X.; Jeong, H.; Oh, S. H.; Ma, M.; Zhang, K.; Kwon, J.; Choi, I. T.; Choi, I. Y.; Kim, H. K.; Kim, J. K.; Park, J. H. Unassisted Photoelectrochemical Water Splitting Exceeding 7% Solar-to-Hydrogen Conversion Efficiency Using Photon Recycling. *Nat. Commun.* **2016**, *7*, 11943.

(30) Zhong, M.; Hisatomi, T.; Kuang, Y.; Zhao, J.; Liu, M.; Iwase, A.; Jia, Q.; Nishiyama, H.; Minegishi, T.; Nakabayashi, M.; Shibata, N.; Niishiro, R.; Katayama, C.; Shibano, H.; Katayama, M.; Kudo, A.; Yamada, T.; Domen, K. Surface Modification of CoO_x Loaded $BiVO_4$ Photoanodes with Ultrathin *p*-Type NiO Layers for Improved Solar Water Oxidation. *J. Am. Chem. Soc.* **2015**, *137*, 5053–5060.

(31) Yamakata, A.; Ranasinghe, C. S. K.; Hayashi, N.; Kato, K.; Vequizo, J. J. M. Identification of Individual Electron- and Hole-Transfer Kinetics at $CoO_x/BiVO_4/SnO_2$ Double Heterojunctions. *ACS Appl. Ener. Mater.* **2020**, *3*, 1207–1214.

(32) Zhao, X.; Lu, Z.; Ma, W.; Zhang, M. ; Ji, R. ; Yi, C. ; Yan, Y. One-step Fabrication of Carbon Decorated $Co_3O_4/BiVO_4$ p-n Heterostructure for Enhanced Visible-light Photocatalytic Properties. *Chem. Phys. Lett.* **2018**, *706*, 440–447.

(33) Petala, A.; Noe, A.; Frontistis, Z.; Drivas, C. ; Kennou, S. ; Mantzavinos, D. ; Kondarides, D. I. Synthesis and Characterization of $CoO_x/BiVO_4$ Photocatalysts for the Degradation of Propyl Paraben. *J. Hazardous. Mater.* **2019**, *372*, 52-60.

(34) Hermans, Y.; Murcia-Lopez, S.; Klein, A.; van de Krol, R.; Andreu, T.; Morante, J. R.; Toupance, T.; Jaegermann, W. Analysis of the Interfacial Characteristics of $BiVO_4$/Metal Oxide Heterostructures and its Implication on their Junction Properties, *Phys. Chem. Chem. Phys.* **2019**, *21*, 5086–5096.

(35) Zachäus, C.; Abdi, F. F.; Peter, L. M. ; van de Krol, R. Photocurrent of $BiVO_4$ is Limited by Surface Recombination, not Surface Catalysis, *Chem. Sci.* **2017**, *8*, 3712–3719.

(36) Seh, Z. W.; Kibsgaard, J.; Dickens, C. F.; Chorkendorff, I.; Nørskov, J. K.; Jaramillo, T. F. Combining Theory and Experiment in Electrocatalysis: Insights into Materials Design. *Science* **2017**, *355 (6321)*, [eaad4998].

(37) Ohno, T.; Sarukawa, K.; Matsumura, M. Crystal Faces of Rutile and Anatase TiO_2 Particles and Their Roles in Photocatalytic Reactions. *New J. Chem.* **2002**, *26*, 1167–1170.

(38) D'Arienzo, M.; Dozzi, M. V.; Redaelli, M.; DI Credico, B.; Morazzoni, F.; Scotti, R.; Polizzi, S. Crystal Surfaces and Fate of Photogenerated Defects in Shape-Controlled Anatase Nanocrystals: Drawing Useful Relations to Improve the H_2 Yield in Methanol Photosteam Reforming. *J. Phys. Chem. C* **2015**, 119, 12385–12393.

(39) Hermans, Y., Klein, A., Sarker, H. P., Huda, M. N., Junge, H., Toupance, T., Jaegermann, W., Pinning of the Fermi Level in $CuFeO_2$ by Polaron Formation Limiting the Photovoltage for Photochemical Water Splitting. *Adv. Funct. Mater*. **2020**, *30*, 1910432.

(40) Wenderich, K.; Mul, G. Methods, Mechanism, and Applications of Photodeposition in Photocatalysis: A Review. *Chem. Rev.* **2016**, *116*, 14587–14619.

(41) Mu, L.; Zhao, Y.; Li, A.; Wang, S.; Wang, Z.; Yang, J.; Wang, Y.; Liu, T.; Chen, R.; Zhu, J.; Fan, F.; Li, R.; Li, C. Enhancing Charge Separation on High Symmetry $SrTiO_3$ Exposed with Anisotropic Facets for Photocatalytic Water Splitting. *Energy Environ. Sci.* **2016**, *9*, 2463–2469.

(42) Kashiwaya, S.; Toupance, T.; Klein, A.; Jaegermann, W. Fermi Level Positions and Induced Band Bending at Single Crystalline Anatase (101) and (001) Surfaces: Origin of the Enhanced Photocatalytic Activity of Facet Engineered Crystals. *Adv. Energy Mater.* **2018**, *8*, 1802195.

(43) Li, R.; Zhang, F.; Wang, D.; Yang, J.; Li, M.; Zhu, J.; Zhou, X.; Han, H.; Li, C. Spatial Separation of Photogenerated Electrons and Holes among {010} and {110} Crystal Facets of $BiVO_4$. *Nat. Commun.* **2013**, *4*, 1432.

(44) Li, R.; Han, H.; Zhang, F.; Wang, D.; Li, C. Highly Efficient Photocatalysts Constructed by Rational Assembly of Dual-cocatalysts Separately on Different Facets of $BiVO_4$. *Ener. Environ. Sci.* **2014**, *7*, 1369–1376.

(45) Chen, X.; Chen, W.; Lin, P.; Yang, Y.; Gao, H.; Yuan, J.; Shangguan, W. In Situ Photodeposition of Nickel Oxides on CdS for Highly Efficient Hydrogen Production via Visible-Light Driven Photocatalysis. *Catal. Commun.* **2013**, *36*, 104–108.

(46) Kashiwaya, S.; Olivier, C.; Majimel, J.; Klein, A.; Jaegermann, W.; Toupance, T. Nickel Oxide Selectively Deposited on the {101} Facet of Anatase TiO_2 Nanocrystal Bipyramids for Enhanced Photocatalysis. *ACS Appl. Nanomater.* **2019**, *2*, 4793–4803.

(47) Choi, S. K.; Choi, W.; Park, H. Solar Water Oxidation Using Nickel-borate Coupled $BiVO_4$ Photoelectrodes. *Phys. Chem. Chem. Phys.* **2013**, *15*, 6499–6507.

(48) Li, C.; Zhang, P.; Lv, R.; Lu, J. ; Wang, T. ; Wang, S. ; Wang, H. ; Gong, J. Selective Deposition of Ag_3PO_4 on Monoclinic $BiVO_4$ (040) for Highly Efficient Photocatalysis. *Small* **2013**, *9*, 3951–3956.

(49) Klein, A. Interface Properties of Dielectric Oxides. *J. Am. Ceram. Soc.* **2016**, *99*, 369–387.

(50) Klein, A. Transparent Conducting Oxides: Electronic Structure-Property Relationship from Photoelectron Spectroscopy with in Situ Sample Preparation. *J. Am. Ceram. Soc.* **2013**, *96*, 331–345.

(51) Su, J.; Zou, X.-X.; Li, G.-D. ; Wei, X. ; Yan, C. ; Wang, Y.-N. ; Zhao, J. ; Zhou, L.-J.; Chen, J.-S. Macroporous V_2O_5-$BiVO_4$ Composites: Effect of Heterojunction on the Behavior of Photogenerated Charges. *J. Phys. Chem. C* **2011**, *115*, 8064–8071.

(52) Lin, H., Ye, H., Chen, S.; Chen, Y. One-pot Hydrothermal Synthesis of $BiPO_4$/$BiVO_4$ with Enhanced Visible-light Photocatalytic Activities for Methylene Blue Degradation. *RSC Adv.* **2014**, *4*, 10968–10974.

(53) Wagner, C.; Naumkin, A.; Kraut-Vass, A.; Allison, J.; Powell, C.; Rumble Jr, J. NIST Standard Reference Database 20, Version 3.4., **2003**.

(54) Moulder, J. F.; Stickle, W. F.; Sobol, P. E.; Bomben, K. D., Handbook of X-ray Photoelectron Spectroscopy: A Reference Book of Standard Spectra for Identi€cation and Interpretation of XPS Data; Physical Electronics: Eden Prairie MN, **1992**, p 261.

(55) Zhu, J.; Fan, F.; Chen, R.; An, H.; Feng, Z.; Li, C. Direct Imaging of Highly Anisotropic Photogenerated Charge Separations on Different Facets of a Single $BiVO_4$ Photocatalyst. *Angew. Chem. Int. Ed.* **2015**, *54*, 9111–9114.

(56) Liu, T.; Zhou, X.; Dupuis, M.; Li, C. The nature of Photogenerated Charge Separation Among Different Crystal Facets of $BiVO_4$ Studied by Density Functional Theory. *Phys. Chem. Chem. Phys.* **2015**, *17*, 23503–23510.

(57) Zhu, J.; Pang, S.; Di.rich, T.; Gao, Y.; Nie, W.; Cui, J.; Chen, R.; An, H.; Fan, F.; Li, C. Visualizing the Nano Cocatalyst Aligned Electric Fields on Single Photocatalyst Particles. *Nano Lett.* **2017**, *17*, 6735–6741.

(58) Biesinger, M. C.; Payne, B. P.; Grosvenor, A. P.; Lau, L. W.; Gerson, A. R.; Smart, R. S. C. Resolving Surface Chemical States in XPS Analysis of First row Transition Metals, Oxides and Hydroxides: Cr, Mn, Fe, Co and Ni. *Appl. Surf. Sci.* **2011**, *257*, 2717–2730.

(59) Mayer, B.; Uhlenbrock, S.; Neumann, M. XPS Satellites in Transition Metal Oxides. *J. Electron. Spectros. Relat. Phenomena* **1996**, *81*, 63–67.

(60) Weidler, N.; Paulus, S.; Schuch, J.; Kle., J.; Hoch, S.; Stenner, P.; Maljusch, A.; Brötz, J.; Wittich, C.; Kaiser, B.; Jaegermann,W. CoO_x Thin Film Deposited by CVD as Efficient Water Oxidation Catalyst: Change of Oxidation State in XPS and its Correlation to Electrochemical Activity. *Phys. Chem. Chem. Phys.* **2016**, *18*, 10708–10718.

(61) Yang, J.; Liu, H.; Martens, W. N.; Frost, R. L. Synthesis and Characterization of Cobalt Hydroxide, Cobalt Oxyhydroxide, and Cobalt Oxide Nanodiscs. *J. Phys. Chem. C* **2010**, *114*, 111–119.

(62) McIntyre, N. S.; Cook, M. G. X-ray Photoelectron Studies on Some Oxides and Hydroxides of Cobalt, Nickel, and Copper. *Anal. Chem.* **1975**, *47*, 2208–2213.

(63) Lin, F.; Boettcher, S. W. Adaptive Semiconductor/electrocatalyst Junctions in Water Splitting Photoanodes. *Nat. Mater.* **2014**, *13*, 81–86.

(64) Grosvenor, A. P.; Biesinger, M. C.; Smart, R. S. C.; McIntyre, N. S. New Interpretations of XPS Spectra of Nickel Metal and Oxides. *Surf. Sci.* **2006**, *600*, 1771–1779.

(65) Biesinger, M. C.; Lau, L.W. M.; Gerson, A. R.; Smart, R. S. C. The role of the Auger Parameter in XPS Studies of Nickel Metal, Halides and Oxides. *Phys. Chem. Chem. Phys.* **2012**, *14*, 2434–2442.

(66) Weidler, N.; Schuch, J.; Knaus, F.; Stenner, P.; Hoch, S.; Maljusch, A.; Schäfer, R.; Kaiser, B.; Jaegermann,W. X-ray Photoelectron Spectroscopic Investigation of Plasma-Enhanced Chemical Vapor Deposited NiO_x, $NiO_x(OH)_y$, and $CoNiO_x(OH)_y$: Influence of the Chemical Composition on the Catalytic Activity for the Oxygen Evolution Reaction *J. Phys. Chem. C* **2017**, *121*, 6455–6463.

(67) Cooper, J.K.; Gul, S.; Toma, F. M.; Chen, L.; Liu, Y.-S.; Guo, J.; Ager, J. W.; Yano, J.; Sharp, I. D. Indirect Bangap and Optical Properties of Monoclinic Bismuth Vanadate. *J. Phys. Chem. C* **2015**, *119*, 2969-2974.

(68) Li, J.; Zhou, J.; Hao, H.; Zhu, F. Silver-modified Specific (040) facet of $BiVO_4$ with Enhanced Photoelectrochemical Performance. *Mater. Lett.* **2016**, *170*, 163–166.

(69) Wu, J.; Wang, Y.; Liu, Z.; Yan, Y.; Zhu, Z. Preparation of Noble Metal Ag-modified $BiVO_4$ Nanosheets and a Study on the Degradation Performance of Tetracyclines. *New J. Chem.* **2020**, *44*, 13815–13823.

(70) Limburg, B.; Bouwmann, E.; Bonnet, S. Molecular Water Oxidation Catalysts Based on Transition Metals and their Decomposition Pathways. *Coord. Chem. Rev.* **2012**, *256*, 1451–1467.

(71) Bratsch, S. G. Standard Electrode Potentials and Temperature Coefficients in Water at 298.15 K. *J. Phys. Chem. Ref. Data* **1989**, *18*, 1–21.

(72) Tan, H. L.; Wen, X.; Amal, R.; Ng, Y. N. $BiVO_4$ {010} and {110} Relative Exposure Extent: Governing Factor of Surface Charge Population and Photocatalytic Activity. *J. Phys. Chem. Lett.* **2016**, *7*, 1400-1405.

(73) Jo, W. J. ; Jang, J.-W. ; Kong, K.-j. ; Kang, H. J. ; Kim, J. Y. ; Jun, H. ; Parmar, K. P. S. ; Lee, J. S. Phosphate Doping into Monoclinic $BiVO_4$ for Enhanced Photoelectrochemical Water Oxidation Activity. *Ang. Chem. Int. Ed.* **2012**, *51*, 3147-3151.

(74) Kong, H. J.; Won, D. H.; Kim, J.; Woo, S. I. Sulfur-Doped g-C_3N_4/$BiVO_4$ Composite Photocatalyst for Water Oxidation under Visible Light. *Chem. Mater.* **2016**, *28*, 1318-1324.

(75) Iwase, A.; Ng, Y. H.; Ishiguro, Y.; Kudo, A.; Amal, R. Reduced Graphene Oxide as Solid State Electron Mediator in Z-Scheme Photocatalytic Water Splitting under Visible Light. *J. Am. Chem. Soc.* **2011**, *133*, 11054-11057.

(76) Melo, M. A.; Wu, Z.; Nail, B. A. ; De Denko, A. T. ; Nogueira, A. F. ; Osterloh, F. E. Surface Photovoltage Measurement on a Particle Tandem Photocatalyst for Overall Water Splitting. *Nano Lett.* **2018**, *18*, 805-810.

(77) Wei, T.; Zhu, Y.-N.; Gu, Z.; An, X.; Liu, L.m.; Wu, Y.; Liu, H.; Tang, J.; Qu, J. Multi-electric Field Modulation for Photocatalytic Oxygen Evolution: Enhanced Charge Separation by Coupling Oxygen Vacancies with Faceted Heterostructures. *Nano Ener.* **2018**, *51*, 764-773.

SYNOPSIS

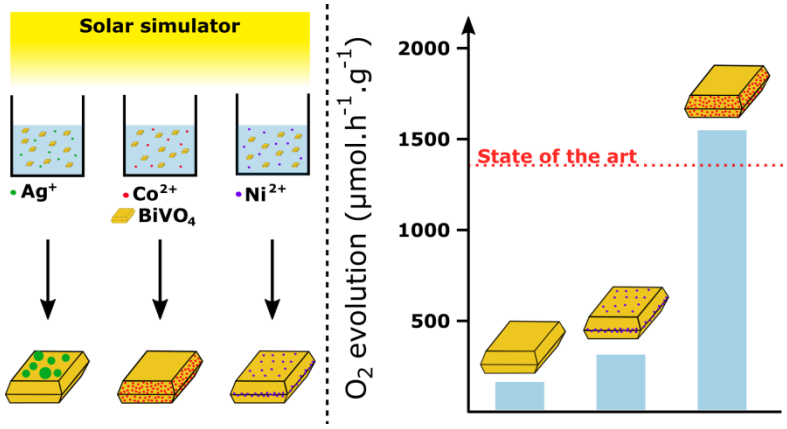
Solar simulator
Ag+
Co2+
BiVO4
Ni2+
O2 evolution (µmol.h-1.g-1)
2000
1500
1000
500
State of the art